Magnetic and Pressure Effects on E–H Mode Transition Power and Electron Energy Distribution in Helical Antenna-Coupled RF Plasma

Chuansheng Wang, Xuhui Liu, Jinyue Geng, Fei Li, Xin Lin, and Xilong Yu

***Abstract*— We used helical antenna-coupled radio frequency (RF) plasmas to study the evolution of the mode transition power and electron kinetics under different applied magnetic fields and argon pressures. Langmuir probe and emission spectrum data indicate that the discharge mode changes from the capacitive coupling E mode to the inductive coupling H mode through a strong mixed mode (E + H). One reason for this strongly mixed ionization is the antenna structure, which increases the capacitive coupling. Furthermore, the E→H transition threshold power decreases with increasing pressure regardless of whether there is a magnetic field, and the presence of the magnetic field significantly increases the transition power. The electron energy distribution function (EEDF) curve has a Druyvesteyn shape at low RF power (E mode). The presence of a magnetic field increases the electron energy range, and the binding of the electrons by the magnetic field causes the EEDF to deviate significantly from the Maxwellian shape. As RF power increases, the EEDF tends toward the Maxwellian shape during the transition from the E mode to the H mode. The magnetic field appears to act like a drag on this process, particularly at very low pressures.**

***Index Terms*— E–H mode transition, electron energy distribution function (EEDF), helical antenna, magnetic.**

I. INTRODUCTION

PLASMA sources need to offer highly efficient ionization and high density for applications, including surface treatment [1], [2] and electrodeless space thrusters [3]–[7]. The helicon plasma source ($\sim 10^{13}$ cm^{-3}) is ideal for satisfying these requirements. Application of an axial magnetic field is essential to the excitation of the helicon wave, and the helical antenna ($m = +1$) is one of the most used antennas [8]–[13] for helicon plasma generation. As the input power increases, the dominant radio frequency (RF) plasma coupling modes are capacitive coupling (E mode: 10^9–10^{11} cm^{-3}), inductive coupling (H mode: 10^{11}–10^{12} cm^{-3}), and, finally, wave coupling (W mode: $\sim 10^{13}$ cm^{-3}) ionization [14]–[18]. In most cases, the plasma parameters show a "jump" at the threshold power [19]–[21]. However, the detailed mechanisms of the mode transitions are not yet fully understood. Many researchers have focused on the wave coupling mode, while the first two modes (the E and H modes) are also significant to helicon plasma initiation [22] because a propagating helicon wave must exist in the plasma, and a mechanism must also exist to preheat the electrons into the traveling wave trap [9], [18]. However, the influence of the applied axial magnetic field on both the mode transition power and the electron energy distribution function (EEDF) has been studied less systematically in helical antenna-coupled plasmas.

Experiments indicate that, in inductively coupled plasma (ICP) [23], [24], the pressure [20], [25], [26], the RF source frequency [27], and the gas composition [28]–[32] all influence the electron density [20], [28], [33], [34], the transition power, and the EEDF [19]–[21], [35]–[38]. Several different mechanisms have been proposed to address this problem. Lieberman [35] and El-Fayoumi [36] indicated that mode jumping and hysteresis are mainly caused by two nonlinear effects. The first effect is the nonlinear absorbed power in the E and H modes. The second effect is the nonlinear plasma power loss [39] that arises from the multistep ionization process. The EEDF can represent the kinetics of the electrons and may vary with the different modes. Singh *et al.* [40] and Park *et al.* [41] have proposed that the EEDF has a bi-Maxwellian shape in the vicinity of the E→H and H→E transitions, while the shape is either Maxwellian or Druyvesteyn (depending on the plasma pressure) in both "pure" modes. Further research has indicated that the electronic response of the plasma cross section to certain energies is strong, which results in nonlinear energy absorption that deforms the EEDF [29], [42], [43]. In addition, the antenna style and size can cause changes in the skin depth, which influences the mode jumping and hysteresis behavior [10], [44]. Lieberman [35], Daltrini *et al.* [45], and Gao *et al.* [46] found that the power loss in the matching box is another important factor. Lee *et al.* [23] demonstrated that the hysteresis disappeared at the automatching ionization condition. These different statements indicate that the mechanism

---

Manuscript received June 17, 2020; revised September 2, 2020, February 2, 2021, and April 16, 2021; accepted May 28, 2021. Date of publication August 13, 2021; date of current version September 15, 2021. This work was supported in part by the National Natural Science Foundation of China under Grant 11927803 and Grant 11802315, in part by the Youth Innovation Promotion Association of Chinese Academy of Sciences (CAS), and in part by the Advanced Space Propulsion Technology Laboratory Open Fund. The review of this article was arranged by Senior Editor S. Portillo. *(Corresponding author: Fei Li.)*

Chuansheng Wang and Xilong Yu are with the State Key Laboratory of High Temperature Gas Dynamics, Institute of Mechanics, Chinese Academy of Sciences (CAS), Beijing 100190, China, and also with the School of Engineering Science, University of Chinese Academy of Sciences, Beijing 100049, China.

Xuhui Liu and Jinyue Geng are with Beijing Institute of Control Engineering, China Academy of Space Technology, Beijing 100190, China.

Fei Li and Xin Lin are with the State Key Laboratory of High Temperature Gas Dynamics, Institute of Mechanics, Chinese Academy of Sciences (CAS), Beijing 100190, China (e-mail: lifei@imech.ac.cn).

Color versions of one or more figures in this article are available at https://doi.org/10.1109/TPS.2021.3101194.

Digital Object Identifier 10.1109/TPS.2021.3101194

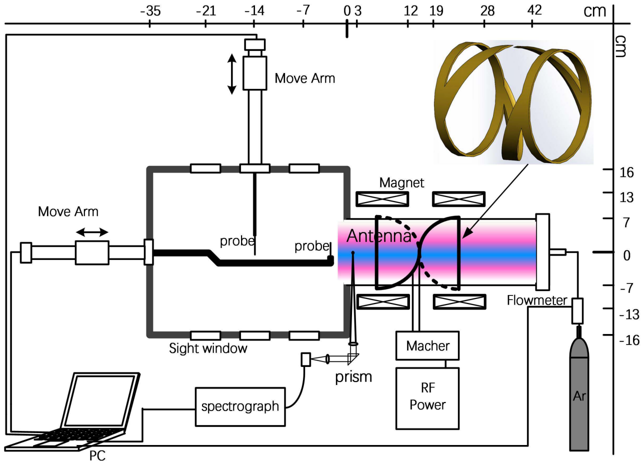

Fig. 1. Schematic of the helicon discharge and diagnostic system.

behind the mode jumps and the hysteresis is unclear in a zero-magnetic-field environment because they do not mention magnetic conditions. Therefore, more experimental studies are needed to understand this phenomenon.

This article studies the relationship between the magnetic field, pressure, and mode transition power in helical antenna-coupled RF plasma. The reasons for the power change of the mode transition are analyzed through the evolution of the EEDF with RF power. For that, an RF-compensated Langmuir probe [47], [48] and local optical-emission spectroscope are used to diagnose the plasma density, EEDF, and 750.4-nm line intensity [45], [49] evolution. This research shows that the E→H transition power decreases with increasing pressure, and the magnetic field causes the transition power to increase. The existence of the magnetic field cannot significantly increase the number density of high-energy electrons. The EEDF has an approximately Druyvesteyn shape at low power and a Maxwellian distribution at high power. The presence of a magnetic field makes the EEDF more inclined to a Druyvesteyn distribution.

This article studies the relationship between the magnetic field, pressure, and mode transition power in helical antenna-coupled RF plasma. The evolution of EEDFs is calculated by the third-order difference method from the RF-compensated Langmuir probe [47], [48] *I*–*V* curve in two magnetic field sittings (0 and 170 Gs) to analyze the mechanism of mode transition and hysteresis. The optical-emission spectroscope [45], [49] is used to diagnose the 750.43-nm spectrum to reflect the evolution of high-energy electrons in the mode transition process. This research shows that E→H mode transition power decreases with pressure increasing, and the magnetic field causes the transition power to increase. The EEDF has an approximately Druyvesteyn shape at low power and a Maxwellian distribution at high power.

II. EXPERIMENTAL SETUP AND DIAGNOSTICS

A. Helicon Plasma Discharge System

Fig. 1 shows a schematic of the helicon plasma experiments. The aluminum alloy vacuum chamber had an outer diameter of 340 mm and a length of 390 mm. The background vacuum of this chamber was approximately 5×10^{-5} Pa. A mechanical pump (TRP-24) and a molecular pump (CFB-600) with pumping speeds of 6 and 600 L/s, respectively, were used to maintain the vacuum. A quartz tube with an outer diameter of 145 mm and a length of 420 mm was used as the ionization tube. This tube was connected to the vacuum chamber at one end and was sealed at the entrance using an aluminum flange. A helical antenna with a length of 170 mm and an outer diameter of 160 mm was placed on the exterior of the quartz tube. A 2-kW, 13.56-MHz RF power supply (IMECAS YF2000) was connected to this antenna through a π-type matching box. Argon was used as the process gas and was controlled using a mass flow controller (Bronkhorst F-201CV-050-AGD-33-V). The chamber pressure could be varied between 0.01 and 10 Pa by simply adjusting the flow rate.

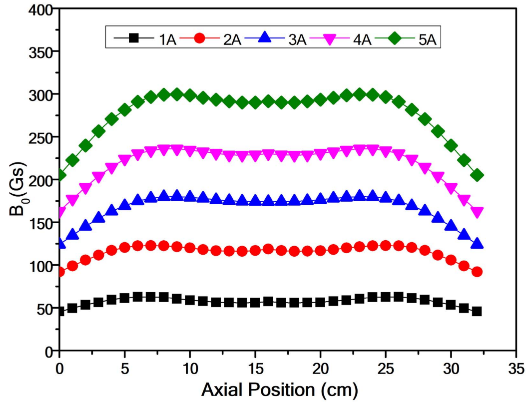

Fig. 2. Axial magnetic field distribution.

The static magnetic field was generated using two electromagnetic coils that were connected in series and enabled sustained operation for more than 1.5 h. The magnetic field intensity could be adjusted between 0 and 300 Gs; the axial field distribution is shown in Fig. 2. As the magnetic field current increases, the maximum magnetic induction intensity increases, and the magnetic field is uniform between 5 and 25 cm.

B. Diagnostic Technology

RF compensation probes were used to diagnose the plasma. Fig. 3(a) shows the typical *I*–*V* curve of this probe. The overall curve is smooth, and the flow of saturated ions is stable. These tungsten probes were 0.3-mm diameter and 8-mm long, and the probe was perpendicular to the magnetic field. A parallel passive RF compensation electrode configuration was used to cancel the plasma potential vibration noise. Filters and isolators were installed in both the scanning circuit and the acquisition circuit to eliminate both RF noise and low-frequency interference. The probe was mounted on a movable arm that had a movement range of 300 mm. The probe was located on the axis of the ionization tube, and the distance to the antenna was approximately 35 mm.

The electron density and the EEDF can be derived from the measured current–voltage (*I*–*V*) curve. The expression for the

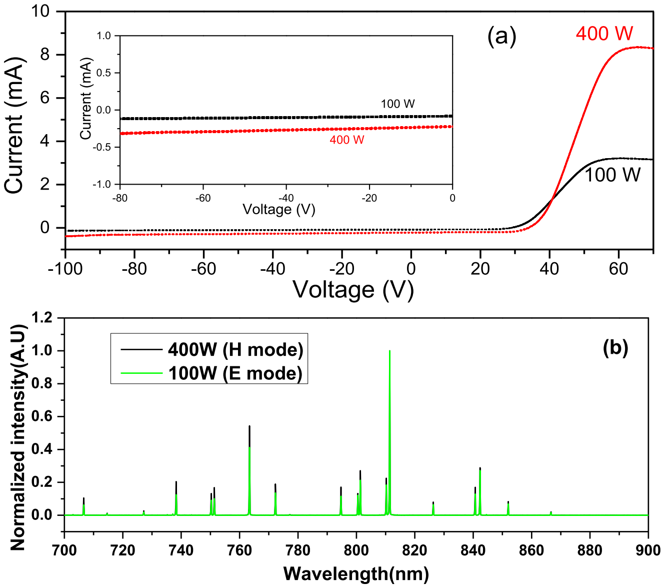

Fig. 3. (a) I–V curve of the probe and (b) emission spectra of the Ar plasma at 2 Pa and 0 Gs for the E mode (100 W) and H mode (400 W).

electron energy probability function (EEPF) is [41]

$$f(\varepsilon)=\frac{2(2m_e)^{\frac{1}{2}}}{e^2A}\cdot\frac{d^2I_e}{dV^2} \tag{1}$$

where ε, e, m_e, I_e, and V are the electron energy, unit charge, electron mass, electron current, and probe bias voltage, respectively; $A = A_s(1+\delta/r)$ is the effective collection area of the probe, where A_s is the probe area, δ is the sheath size, and r is the probe characteristic size. The second derivative of the I–V curve is calculated by the third-order precision finite difference method, and the specific process is given as follows [50].

To start with, the second derivative of the point numbered j can be obtained by a linear combination of the points numbered $j-2$, $j-1$, j, and $j+1$

$$\left(\frac{d^2I_e}{dV^2}\right)_j = a_1I_{ej-2}+a_2I_{ej-1}+a_3I_{ej}+a_4I_{ej+1}+O(V) \tag{2}$$

where a_i is the coefficient to be determined. Then, carry out Taylor expansion of the right term of (2)

$$\begin{aligned}
&a_1I_{ej-2}+a_2I_{ej-1}+a_3I_{ej}+a_4I_{ej+1}\\
&=(a_1+a_2+a_3+a_4)I_{ej}\\
&\quad+[(V_{j-2}-V_j)a_1+(V_{j-1}-V_j)a_2+(V_j-V_j)a_3\\
&\qquad+(V_{j+1}-V_j)a_4]\left(\frac{dI_e}{dV}\right)_j\\
&\quad+\frac{1}{2!}[(V_{j-2}-V_j)^2a_1+(V_{j-1}-V_j)^2a_2+(V_j-V_j)^2a_3\\
&\qquad+(V_{j+1}-V_j)^2a_4]\left(\frac{d^2I_e}{dV^2}\right)_j\\
&\quad+\frac{1}{3!}[(V_{j-2}-V_j)^3a_1+(V_{j-1}-V_j)^3a_2+(V_j-V_j)^3a_3\\
&\qquad+(V_{j+1}-V_j)^3a_4]\left(\frac{d^3I_e}{dV^3}\right)_j.
\end{aligned} \tag{3}$$

The coefficient can be determined by solving the following equation:

$$\begin{cases}
0=a_1+a_2+a_3+a_4\\
0=(V_{j-2}-V_j)a_1+(V_{j-1}-V_j)a_2+(V_j-V_j)a_3\\
\qquad+(V_{j+1}-V_j)a_4\\
1=(V_{j-2}-V_j)^2a_1+(V_{j-1}-V_j)^2a_2+(V_j-V_j)^2a_3\\
\qquad+(V_{j+1}-V_j)^2a_4\\
0=(V_{j-2}-V_j)^3a_1+(V_{j-1}-V_j)^3a_2+(V_j-V_j)^3a_3\\
\qquad+(V_{j+1}-V_j)^3a_4.
\end{cases} \tag{4}$$

Finally, EEPF can be obtained by substituting the calculated coefficients and (2) into (1). The EEDF can be calculated through the expression $F(\varepsilon)=\sqrt{\varepsilon}f(\varepsilon)$. The expression for the electron density is $n_e=\int_0^\infty\sqrt{\varepsilon}f(\varepsilon)d\varepsilon$.

In low-pressure RF plasma, electron impact excitation from the ground state or excited states (Ar*) is the dominant excitation channel to produce plasma. When deexcitation of excited atoms releases photons, the emission intensity I_{ij} with which state j decays to state i is $I_{ij}=K_{ij}A_{ij}n_{\mathrm{Ar}^*}\mathrm{hc}/\lambda$ [51], where K_{ij} is the spectrometer factor, A_{ij} is the Einstein coefficient, n_{Ar^*} is the Ar* level density, c is the velocity of vacuum light, h is the Planck constant, and λ is the wavelength. A telescope system and an aperture grating were then used to collect the plasma emission light emitted at the probe position for input into an Avaspec four-branched multichannel spectrometer (AvaSpecULS3648) with a resolution of 0.1 nm [at its full-width at half-maximum (FWHM)] and an acquisition spectral range between 390 and 900 nm. The plasma line mainly comes from the transition between the $4p$ state and the $4s$ state of argon atoms that are concentrated at 700–900 nm, as shown in Fig. 3(b).

III. RESULTS AND ANALYSIS

A. E–H Mode Transition Characteristics

For this study, the six set pressure conditions, 0.5, 2, 4, 6, 9, and 10 Pa, were used. As shown in Fig. 4, when the magnetic field is higher than 200 Gs, the morphology of the I–V curve is deformed. Therefore, in order to reduce the complexity of I–V curve correction, a magnetic field condition of 170 Gs was selected in our experiments. The zero magnetic field operating condition was used as a comparative experiment.

The change in the electron density with varying RF power is usually used to explain the mode transition and hysteresis properties. Fig. 5 shows the change in the electron density with power under a zero magnetic field. The E–H mode transition appears with power increase, and the transform shape is different with pressure increased. For example, at 0.5 Pa, the electron density increases rapidly when the power reaches 130 W. This transition occurs at a different power for each pressure, as shown by the segmented blue line in each graph; this represents the E–H mode transition. At higher pressures, the electron density curve contains an ionization interval with a greater slope, as shown by the next segment of the blue line in each graph. The mode transitions in Fig. 5 occur through a mixed mode, E + H. In each graph, the zone of the mixed mode is between the vertical red line and the vertical green

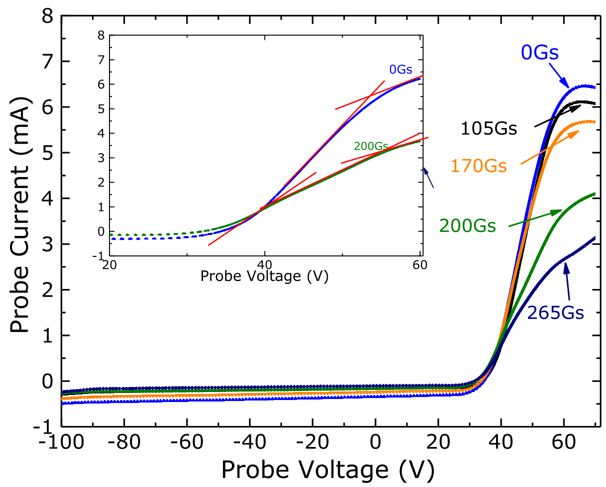

Fig. 4. I–V curve variation with magnetic field intensity, $P_{\mathrm{rf}} = 300$ W.

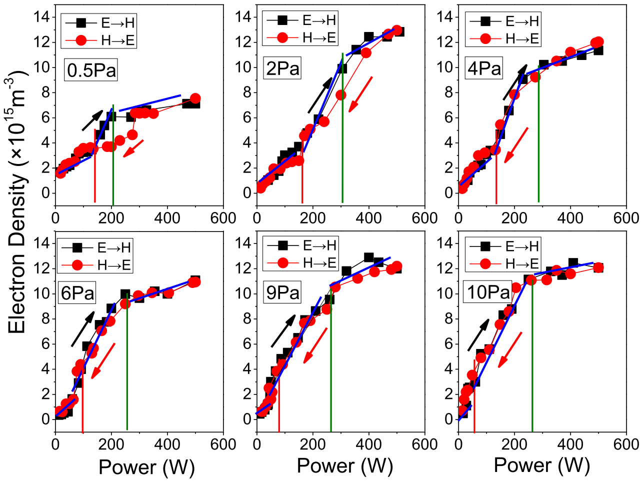

Fig. 5. Curves of electron density versus power at different discharge pressures. The location of the vertical red line represents the E→H transition power and the beginning power of the mixed mode, and the green line is at the end power of the mixed mode. The segmented blue line indicates the mode transition profile. $B = 0$ Gs in all cases.

line. As the ionization pressure increases, the E→H mode transition threshold decreases, and the mixed-mode section expands. When the pressure is lower than 2 Pa, a slight antihysteresis occurs during the E–H–E mode transition. A 130-W antihysteresis zone appears at 0.5 Pa. In contrast, there is no hysteresis at high pressures. One reason for these phenomena is the increased capacitive coupling caused by the antenna structure, which will be analyzed in detail in Section IV-A.

Fig. 6 shows the electron density at different pressures and RF powers under an applied magnetic field of 170 Gs. The E–H mode transition phenomenon and hysteresis loop are appearing. In the E mode, the electron density increases slowly with increasing power. When the power exceeds the mode transition threshold, the electron density rises rapidly, and then, the discharge enters the H mode. As the discharge pressure rises, the efficiency of the generation of metastable particles increases, resulting in that the contribution of multistep ionization to the total ionization increases with the increase in discharge pressure. Therefore, the power entering the H-mode discharges decreases from about 600 W at 0.5 Pa to about 250 W in 10 Pa. The difference in the electron density between E and H modes is increasing with pressure increasing.

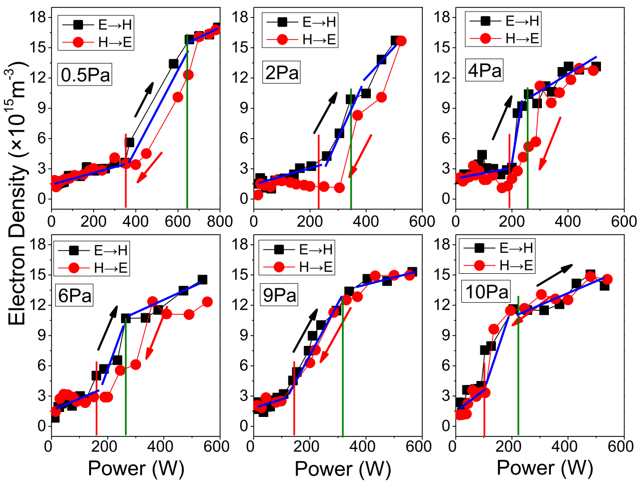

Fig. 6. Curves of electron density versus power at different discharge pressures. The location of the vertical red line represents the E→H transition power and the beginning power of the mixed mode, and the green line is at the end power of the mixed mode. The segmented blue line is illustrating the mode transition profile. $B = 170$ Gs in all cases.

By comparing Fig. 5 with Fig. 6, it is found that, when the magnetic field is zero, there is a larger energy interval between E and H modes, while, at 170 Gs, when the RF power exceeds the E→H transition threshold, the electron density jumps. At 170 Gs, a complete hysteresis loop in the discharge pressure range from 0.5 to 6 Pa is appearing, while it has a complete hysteresis loop only in 0.5-Pa discharge pressure case in the 0-Gs case. The analysis suggests that the addition of a magnetic field leads to a reduction in the radial loss of electrons, the electrons undergo cyclotron motion under the restraint of the magnetic field, and the nonlinear action inside the plasma increases, resulting in a discharge with a magnetic field significantly different from a discharge without a magnetic field.

B. High-Energy Electron Response to Magnetic Intensity

The change in the Ar I 750.4 nm/pressure intensity is generally used to characterize the change in the number of high-energy electrons. The intensity value is acquired by integrating the spectral outline. The maximum intensity in the 0-Gs, 0.5-Pa ionization case is used for normalization. Fig. 7 shows the normalized 750.4-nm/pressure line intensity as a function of power. The curves show that, as the ionization power increases, the number of high-energy electrons also increases. At the same power, the number of high-energy electrons decreases as the gas pressure increases. With the presence of a magnetic field, the acceleration distance of electrons between two adjacent collisions and the efficiency of generating high-energy electrons will reduce [28]. Therefore, the intensity of the spectral line at the same discharge pressure is lower than that without a magnetic field, as shown in Fig. 7(a) and (b). It indicates that the magnetic field has an inhibitory effect on high-energy electrons. When the

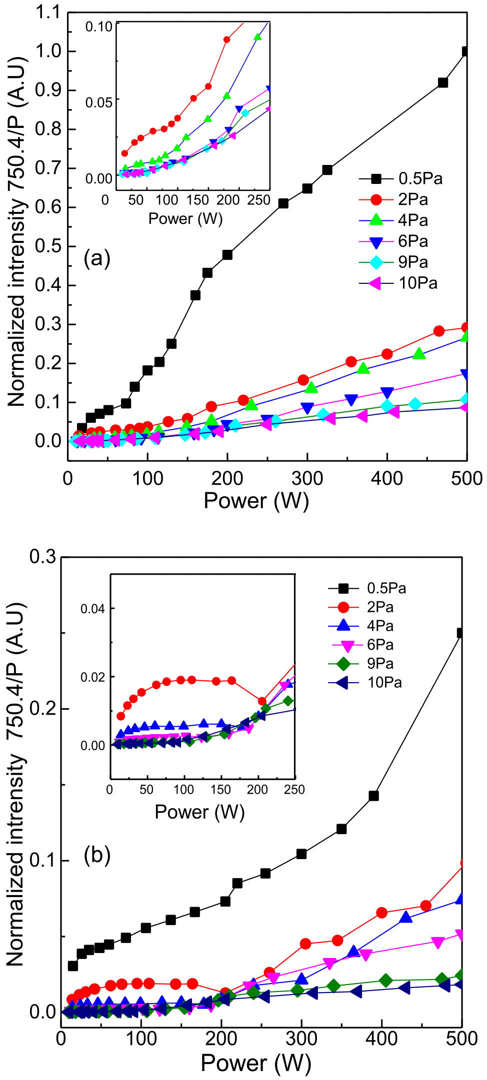

Fig. 7. Normalized emission intensity of Ar I 750.4 nm/pressure line at different RF powers. (a) $B = 0$ Gs. (b) $B = 170$ Gs.

magnetic field is zero at a pressure of 0.5 Pa, the spectral line intensity increases gradually in E and H modes, respectively, while, at the 170-Gs case, the spectral line intensity increases slowly with increasing power in the E mode. The rapid increase is appearing when RF power is higher than the E→H transition threshold. As shown in Fig. 7(b), the density of high-energy electrons increases rapidly at high input power when magnetic field exists. It is shown in Fig. 7(b) that, when ionization is approaching the E–H mode transition threshold, the intensity of the 750.43/Pa line decreases with the power increase, while this phenomenon is missing in Fig. 7(a). One possible reason is that the magnetic field increases the inductive coupling component at the E→H mode transition point, and the inductive coupling mainly produces low-energy electrons. The electron density is approximately constant at the mode transition point. It means that high-energy electrons will decrease. The other reason is that, when the magnetic field has been added into the plasma, the collision frequency of electron–electron and electron–neutral particles will increase. It increases the efficiency of energy transformation and leading to the loss of high-energy electrons. Finally, the intensity of the spectral line decreases with the increase in power.

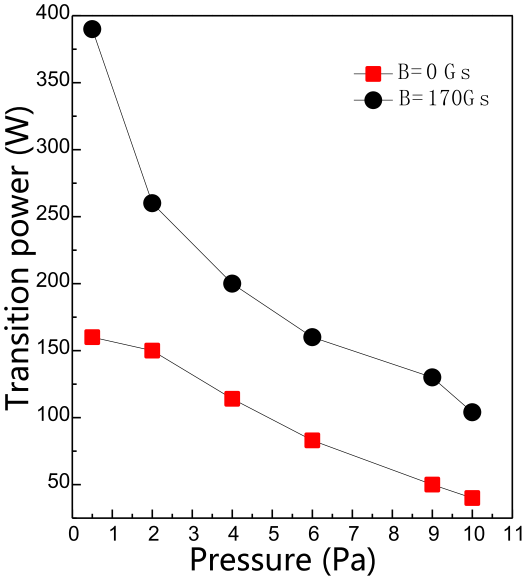

Fig. 8. Measured E→H transition power as a function of pressure at $B = 0$ and 170 Gs.

C. Analysis of Transition Power

Fig. 8 shows the transition power characteristics under different pressures and magnetic fields. The curve shows that the E→H threshold decreases continuously as the pressure increases from 0.5 to 10 Pa. When the magnetic field is 170 Gs, the threshold power of the E→H mode transition is significantly higher than the corresponding value for the zero-magnetic-field cases under the same pressures. The magnetic field causes the electrons to drive the Lamor cyclotron. The motion of the electrons in the plasma sheath is the Hall motion under the combined action of the electric field and the magnetic field. The sheath structure then deviates seriously from the classic form (a periodic dynamic sheath containing RF vibration) as a result. In addition, the binding of the electrons by the magnetic field is equivalent to an increase in the local electron density, which leads to an increase in the sheath thickness, that is, an increase in the equivalent capacitive coupling. All of these cause the capacitive power transition to increase and have nonlinear characteristics [52]. Therefore, the E→H threshold power increases in the $B = 170$ Gs cases. As pressure increases, the frequency of the electron–neutral particle collisions increases, and the energy transfer efficiency also increases, which means that the generation of high-energy electrons becomes difficult. The overall effect of the magnetic field on the electrons is, thus, weakened, which results in the transition power decreasing with increasing pressure.

D. Analysis of the EEDF Evolution

The EEDF generally contains key information about a plasma (such as the reaction kinetics and diffusion characteristics) and can be used to analyze the plasma chemical reactions [41]. The distribution shape of EEDF is determined by the fitting method; typical results are shown in Fig. 9.

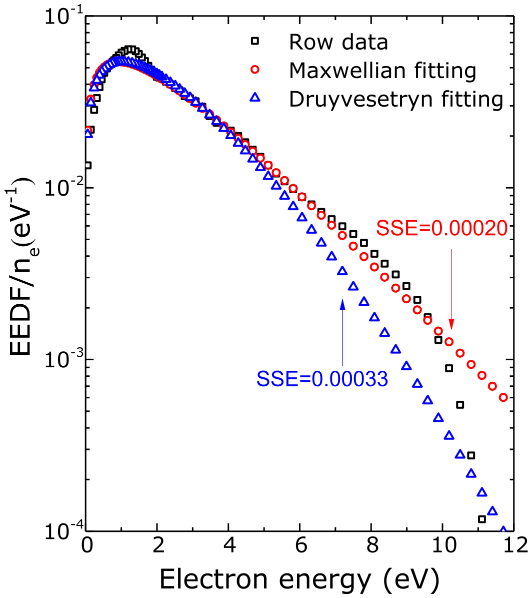

Fig. 9. EEDF diagnostic curve and theoretical fitting curve.

The goodness of fitting is evaluated using the sum of squares due to error (SSE), and the best fitting curve is treated as the shape of EEDF.

The power supply used in this experiment can only be adjusted to some specific gears. Different plasma characteristics could cause different impedances changing the power output of the power supply. Therefore, the power values are incongruent in different experimental states in our experiments.

Fig. 10 shows the evolution of the EEDF during the E-to-H transition at various pressures with $B = 0$ Gs. The EEDF shows a Druyvesteyn shape at low RF power under a pressure of 0.5 Pa, as shown in Fig. 10(a). The number of low-energy electrons (<5 eV) increases and the shape of EEDF changes gradually to Maxwellian when RF power increases. At higher pressure, such as 6 and 9 Pa, the EEDF gradually evolves from a Druyvesteyn shape into a Maxwellian shape as the RF power increases. The number of electrons with energies less than 3 eV increases rapidly, and the proportion of high-energy electrons (>5 eV) decreases. Therefore, the maximum electronic energy (Te-max) of the EEDF curve moves toward the lower energy direction. This process corresponds exactly to the E-to-H mode conversion illustrated in Fig. 5. At a fixed high power, the effective electron temperature decreases with increasing pressure. One of the most important reasons for this behavior is the energy transfer that occurs because of the increase in the frequency of electron–neutral particle collisions, which will be described later in this article. At pressures higher than 4 Pa, the EEDF indicates a sudden reduction in the number of high-energy electrons at around 100 W. The electron temperature decreases with increasing power at the same pressure.

The energetic electron trail also affects the EEDF [52]. Stochastic heating is one of the main ways in which high-energy electrons are generated during E mode ionization. Because of the low electron density, some high-energy electrons reach the wall and are lost without collisions with other electrons. For the cases in this study, this loss in the energetic electron population at the wall is an essential process, and the low electron–electron collision frequency causes inefficient energy transfer between the electrons [53]. Therefore, the wall loss and the low electron–electron collision frequency make the EEDF deviate from the Maxwellian distribution. When the electron density and the pressure increase, the frequency of electron–electron collisions also rises. The shorter electron relaxation distance then reduces the wall loss of high-energy electrons [28], and the EEDF then shows a Maxwellian distribution at high RF power.

Fig. 11 shows the evolution of the EEDF during the E-to-H transition at various pressures with $B = 170$ Gs. When Fig. 11 is compared with Fig. 10, it is obvious that the magnetic field has a great effect on the EEDF. Under the 0.5-Pa ionization illustrated by Fig. 11(a), the EEDF form remains basically unchanged with increasing power. The numbers of high- and low-energy electrons increase synchronously. In contrast to the zero-magnetic-field cases, the effective electron temperature increases at all pressures, and the proportion of high-energy electrons is then higher at the same power. At 6, 9, and 10 Pa, the EEDF tends to change from a Druyvesteyn shape (caused by the elastic collision of electrons and neutral particles [52]) to a Maxwellian distribution with increasing power.

The presence of the magnetic field leads to an anisotropic electron distribution, while the ion distribution can still be considered quasi-isotropic. The exchange of electron energies along the radial direction is limited, but this exchange is not limited axially. This means that the collected electrons will show significantly different distributions because of the different effects of the magnetic field. Therefore, the measured EEDF shows a Druyvesteyn distribution, which causes the effect of the magnetic field to be more remarkable at lower pressures. In the high-pressure cases, e.g., 10 Pa, the electron–electron collision frequency is high enough to lead to approximately Maxwellian distributions in the H mode.

Fig. 12 shows the EEDF evolution when the RF power is reduced. Fig. 12(a) shows the results at $B = 0$ Gs, while Fig. 12(b) shows the corresponding results at $B = 170$ Gs. The Maxwellian distribution appears at high RF power (i.e., in the H mode). At pressures exceeding 0.5 Pa, the EEDF evolves from a high-power Maxwellian distribution to a low-power Druyvesteyn shape as the power decreases. The development of the EEDF is similar to the inverse of the E→H process, i.e., the shape gradually deviates from the Maxwellian distribution. Comparing Figs. 10–12 shows that, during the E→H and H→E transitions, the EEDF cannot completely overlap within the transition region under the same RF power. The expression of the reaction rate K_{ab} is $K_{ab} = \int_0^\infty (\varepsilon/2m)^{(1/2)} Q(\varepsilon) f(\varepsilon) d\varepsilon$, where $Q(\varepsilon)$ represents the cross section, ε is the electron energy, m is the electron mass, and subscripts a and b represent different states. For a certain reaction, the curve profile of the cross section variation with electron energy should be fixed. While the real EEDF will deviate from the Maxwell distribution, so, even if the electron temperature is the same, the reaction rate coefficient K_{ab} obtained by the normalized EEDF integration could be different [52], [54]. Therefore,

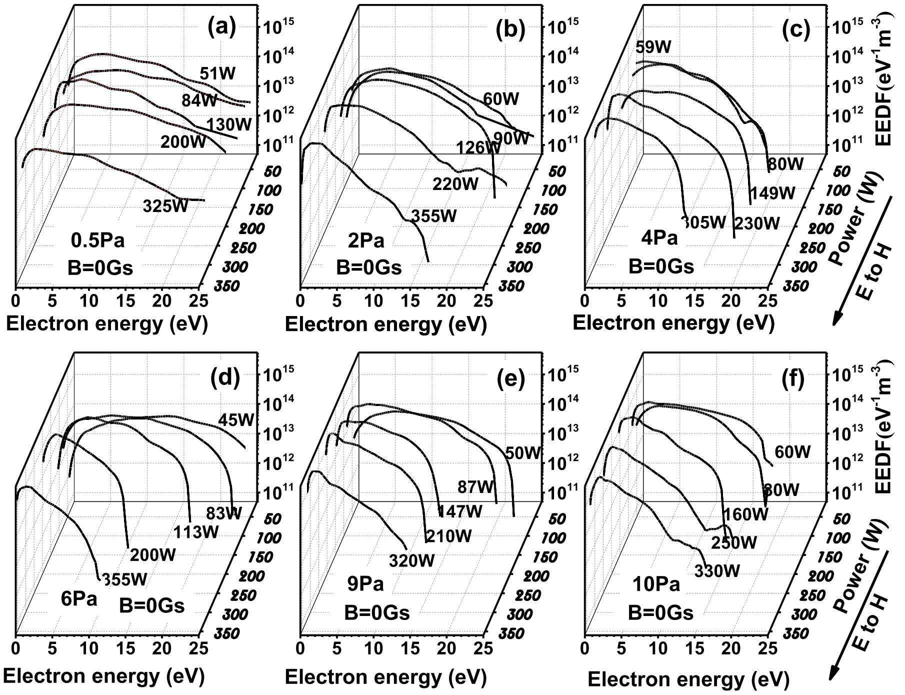

Fig. 10. The EEDF evolution during the E→H mode transition with $B = 0$ Gs at different gas pressures, (a) 0.5 Pa, (b) 2 Pa, (c) 4 Pa, (d) 6 Pa, (e) 9 Pa, (f) 10 Pa.

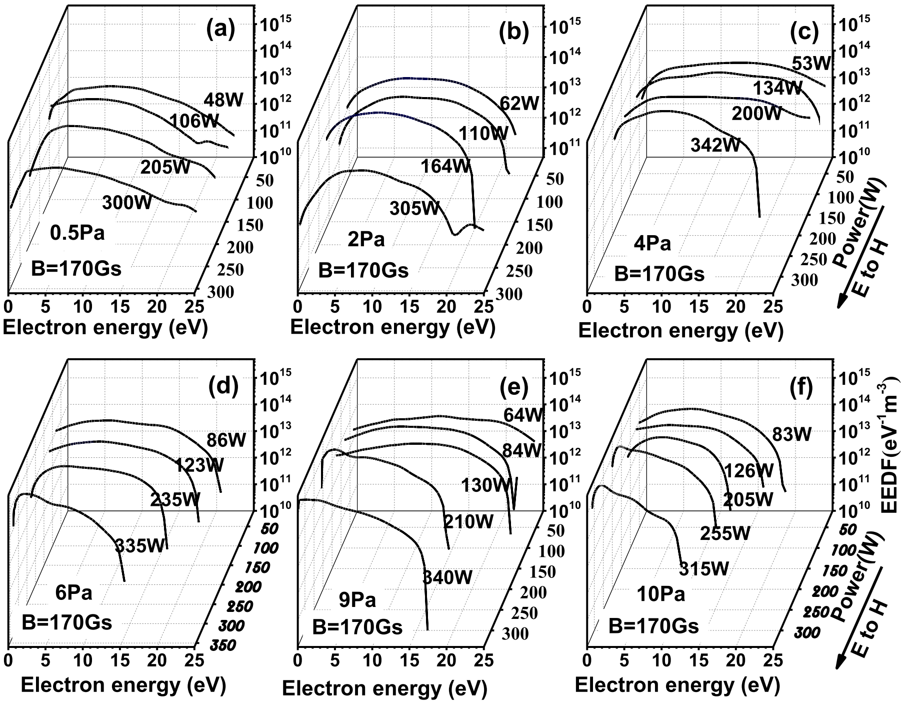

Fig. 11. The EEDF evolution during the E→H mode transition with $B = 170$ Gs at different gas pressures, (a) 0.5 Pa, (b) 2 Pa, (c) 4 Pa, (d) 6 Pa, (e) 9 Pa, (f) 10 Pa.

the ratios of the different channels (e.g., direct ionization and multistep ionization) that generate the plasma will be different in these two transitions. This causes the ionization efficiency to change, which results in hysteresis.

According to [55], the lower the magnetic field, the smaller the influence of the magnetic field on the collected current of the probe. However, the diagnosis result does not affect the regulation of mode transition to the change of magnetic field. Fig. 13 shows the measured evolution curve of EEDF with a magnetic field. The evolution of 300-W working conditions is used to characterize the change of EEDF with magnetic field in the H mode, and 150 W is used to characterize the evolution of EEDF with a magnetic field near the mode transition point. It can be seen from Fig. 13(a) that, when the

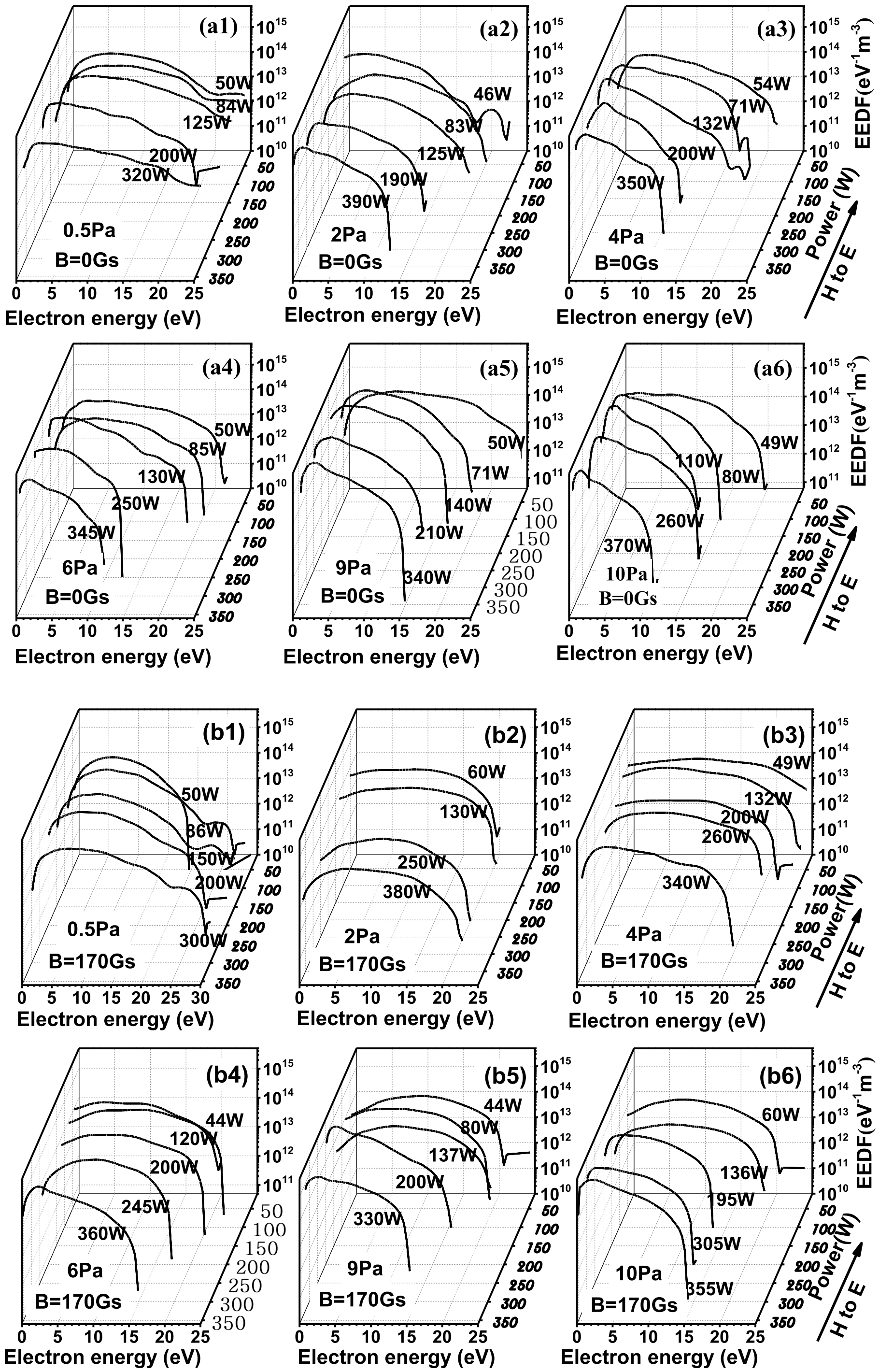

Fig. 12. EEDF evolution during the H→E mode transition, where (a) $B = 0$ Gs and (b) $B = 170$ Gs.

magnetic field is 0 Gs, the EEDF is close to the Maxwellian distribution, and when the magnetic field is increased to 170 Gs, the electron lifetime increases, the electron–neutral collision is enhanced, and the EEDF presents an approximate Druyvesteyn distribution, so the increase in the magnetic field will seriously affect the atomic reaction process at E→H transition point. In Fig. 13(b), when the 300-W discharge is performed, the increase in the magnetic field mainly causes the low-energy electron peak to shift to the high-energy direction, while the EEDF distribution shape shows a tendency to deviate from the Maxwellian morphology. Still, the change is small indicating that the atomic reaction process of sustaining the discharge in a different magnetic field is similar.

IV. DISCUSSION

A. Effect of Helical Antenna on Special Mode Transition

The antenna structure causes the ratio of the capacitive coupling and the inductive coupling to the total energy to change,

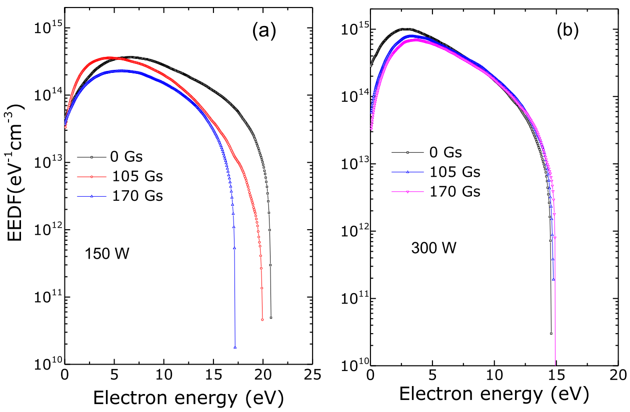

Fig. 13. EEDF evolution with increasing magnetic field intensity at 4 Pa. (a) 150 W. (b) 300 W.

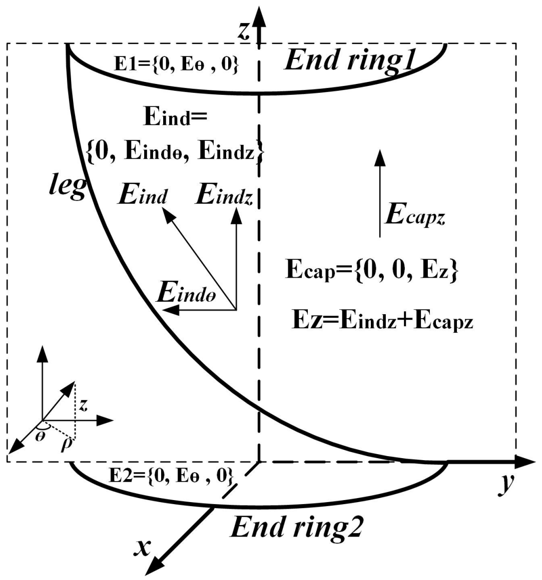

Fig. 14. Schematic of the electric and magnetic fields excited by the helical antenna.

which is one of the reasons for this special characteristic where the electron density changes with the power. A schematic of the helical antenna is shown in Fig. 14. The inductive coupling includes the induced electric fields $\overrightarrow{E_1}$ and $\overrightarrow{E_2}$ generated by the coil at the end of the antenna, both of which are only angular components $\overrightarrow{E_\varphi}$. The field $\overrightarrow{E_{\mathrm{ind}}}$ is generated by the antenna legs, and $\overrightarrow{E_{\mathrm{ind}}} = \overrightarrow{E_{\mathrm{ind}\theta}} + \overrightarrow{E_{\mathrm{ind}z}}$. The axial component $\overrightarrow{E_{\mathrm{ind}z}}$ cannot be ignored, which is unlike the fields of traditional antennas (plate or coil antennas) [23]. The axial electric field that provides capacitive coupling has two components. First, the axial part generated by the voltage difference includes both the traditional capacitive coupling generated by the spiral legs and the electrostatic coupling caused by the inherent resistance of the antenna end ring, $\overrightarrow{E_{\mathrm{cap}z}}$. The other part is the axial component of the electric field induced by the helical antenna's legs, $\overrightarrow{E_{\mathrm{ind}z}}$, whose effect is equivalent to capacitive coupling. Here, $\overrightarrow{E} = \overrightarrow{E_{\mathrm{cap}z}} + \overrightarrow{E_{\mathrm{ind}z}}$, which means that this type of antenna will produce a larger P_{cap}. The capacitive coupling caused by the helical antenna becomes stronger. The power range from capacitive coupling to inductive coupling becomes greater, which results in a greater mixed-mode range.

B. Relationship Between the Ionization Process and the EEDF Distribution

As shown in the evolution of the EEDF during the E→H transition (see Figs. 10 and 11), the proportion of high-energy electrons is high at low RF power, which indicates that direct ionization is the main reason why the ionization is maintained, and the electron density increases slowly. The plasma density is much higher at high RF power than at low-RF-power ionization. This increases the electron–electron collision frequency and increases the efficiency of energy transfer between electrons. Furthermore, the proportion of high-energy electrons is reduced. As a result, the electrons tend toward an equilibrium distribution. Therefore, the proportion of direct ionization in the total ionization also decreases. In contrast, because of the high ionization efficiency of the multistep ionization process, this proportion should increase with increasing power to maintain the rapid increase in the electron density.

When compared with the EEDF evolution under low pressure, the downward trend for the high-energy electrons accelerates at higher pressure as the power increases. The electron density also increases rapidly during this process. Therefore, the contribution of the multistep ionization channel to the total ionization must increase.

High-energy electrons are produced more efficiently when a magnetic field is applied. Hence, direct ionization makes a greater contribution under the same power. This means that the multistep ionization is suppressed by the magnetic field, which causes the electron density to increase slowly and leads to an inefficient discharge state for the E mode. Finally, a special mode transition and hysteresis appear in the E–H–E transition. Comparing Figs. 10 and 11 shows that applying the magnetic field significantly increases the proportion of high-energy electrons in the entire discharge power range. The proportion of high-energy electrons is higher, especially at low pressure and low power. This means that, if the magnetic field continues to increase, the proportion of high-energy electrons to the total electrons continues to increase, especially at low pressure. High-energy electrons are conducive to generating helicon mode ionization. This result partly explains why helicon ionization is more likely at low pressure and a high magnetic field.

V. CONCLUSION

This article studied the E–H mode transition power and EEDF evolution under various magnetic intensities and pressures in helical antenna-coupled plasmas. The antenna structure increased the capacitive coupling, which caused a strong mixed mode. The transition power decreased with increasing pressure. At $B = 170$ Gs, the E→H mode transition power was significantly higher than in the $B = 0$ Gs cases under the same pressure, and the transition power decreased continuously with increasing pressure. The binding of the electrons by the magnetic field is equivalent to increasing the local electron density, which leads to an increase in sheath thickness.

Therefore, the interaction between the magnetic field and the sheath causes an increase in capacitive coupling.

The EEDF curve showed a Druyvesteyn shape at low RF power (E mode) and an expanded electron energy interval that caused the EEDF to deviate greatly from the Maxwellian shape when the magnetic field was applied. When the power was increasing and the pressure was greater than 2 Pa, the EEDF evolved toward the Maxwellian shape with the E-to-H transition, which implies that increased electron–electron collisions cause the electrons to tend toward equilibrium. It was difficult to realize a Maxwellian distribution at lower pressure (<2 Pa) when $B = 0$ Gs. At $B = 170$ Gs, the magnetic field significantly binds the electrons, which increases the frequency of electron–neutral collisions and makes the EEDF tend toward the Druyvesteyn distribution.

REFERENCES

[1] M. Černák, J. Ráhel', D. Kováčik, M. Šimor, A. Brablec, and P. Slavíček, "Generation of thin surface plasma layers for atmospheric-pressure surface treatments," *Contrib. Plasma Phys.*, vol. 44, no. 56, pp. 492–495, Sep. 2004.

[2] W. Leahy *et al.*, "Plasma surface treatment of aerospace materials for enhanced adhesive bonding," *J. Adhes.*, vol. 77, no. 3, pp. 215–249, Sep. 2006.

[3] A. V. Arefiev and B. N. Breizman, "Theoretical components of the VASIMR plasma propulsion concept," *Phys. Plasmas*, vol. 11, no. 5, pp. 2942–2949, May 2004.

[4] R. W. Boswell *et al.*, "Experimental evidence of parametric decay processes in the variable specific impulse magnetoplasma rocket (VASIMR) helicon plasma source," *Phys. Plasmas*, vol. 11, no. 11, pp. 5125–5129, Nov. 2004.

[5] C. Charles, R. W. Boswell, and M. A. Lieberman, "Xenon ion beam characterization in a helicon double layer thruster," *Appl. Phys. Lett.*, vol. 89, no. 26, 2006, Art. no. 261503.

[6] F. R. C. Díaz, "An overview of the VASIMR engine: High power space propulsion with RF plasma generation and heating," in *Proc. AIP Conf.*, 2001, pp. 3–15.

[7] X. Zhang *et al.*, "Pressure dependence of an ion beam accelerating structure in an expanding helicon plasma," *Phys. Plasmas*, vol. 25, no. 2, pp. 1–8, Feb. 2018.

[8] F. F. Chen, "The low-field density peak in helicon discharges," *Phys. Plasmas*, vol. 10, pp. 2586–2592, May 2003.

[9] G. Chen, A. V. Arefiev, R. D. Bengtson, B. N. Breizman, C. A. Lee, and L. L. Raja, "Resonant power absorption in helicon plasma sources," *Phys. Plasmas*, vol. 13, no. 12, Dec. 2006, Art. no. 123507.

[10] V. K. A. G. G. Borg, "An evaluation of different antenna designs for helicon wave excitation in a cylindrical plasma source," *Phys. Plasmas*, vol. 3, pp. 4395–4408, Sep. 1996.

[11] M. D. Carter *et al.*, "Comparing experiments with modeling for light ion helicon plasma sources," *Phys. Plasmas*, vol. 9, no. 12, pp. 5097–5110, Dec. 2002.

[12] S. Shinohara and K. Yonekura, "Discharge modes and wave structures using loop antennae in a helicon plasma source," *Plasma Phys. Controlled Fusion*, vol. 42, no. 1, pp. 41–56, Jan. 2000.

[13] S.-M. Yun, J.-H. Kim, and H.-Y. Chang, "Frequency dependence of helicon wave plasmas near lower hybrid resonance frequency," *J. Vac. Sci. Technol. A: Vac., Surf., Films*, vol. 15, no. 3, pp. 673–677, May 1997.

[14] G. Zhao, H. Wang, X. Si, J. Ouyang, Q. Chen, and C. Tan, "The discharge characteristics in nitrogen helicon plasma," *Phys. Plasmas*, vol. 24, no. 12, Dec. 2017, Art. no. 123507.

[15] R. L. Kinder, A. R. Ellingboe, and M. J. Kushner, "H- to W-mode transitions and properties of a multimode helicon plasma reactor," *Plasma Sources Sci. Technol.*, vol. 12, no. 4, pp. 561–575, Nov. 2003.

[16] G. S. Eom, J. Kim, and W. Choe, "Wave mode conversion and mode transition in very high radio frequency helicon plasma," *Phys. Plasmas*, vol. 13, no. 7, Jul. 2006, Art. no. 073505.

[17] K. P. Shamrai, "Stable modes and abrupt density jumps in a helicon plasma source," *Plasma Sources Sci. Technol.*, vol. 7, no. 4, pp. 499–511, Nov. 1998.

[18] A. R. Ellingboe and R. W. Boswell, "Capacitive, inductive and helicon-wave modes of operation of a helicon plasma source," *Phys. Plasmas*, vol. 3, no. 7, pp. 2797–2804, Jul. 1996.

[19] T. Wegner, C. Küllig, and J. Meichsner, "On the E-H transition in inductively coupled radio frequency oxygen plasmas: I. Density and temperature of electrons, ground state and singlet metastable molecular oxygen," *Plasma Sources Sci. Technol.*, vol. 26, no. 2, Jan. 2017, Art. no. 025006.

[20] J. Wang *et al.*, "E→H mode transition density and power in two types of inductively coupled plasma configuration," *Phys. Plasmas*, vol. 21, no. 7, Jul. 2014, Art. no. 073502.

[21] A. M. Daltrini, S. A. Moshkalev, M. J. R. Monteiro, E. Besseler, A. Kostryukov, and M. Machida, "Mode transitions and hysteresis in inductively coupled plasmas," *J. Appl. Phys.*, vol. 101, no. 7, Apr. 2007, Art. no. 073309.

[22] A. R. Ellingboe, R. W. Boswell, J. P. Booth, and N. Sadeghi, "Electron beam pulses produced by helicon-wave excitation," *Phys. Plasmas*, vol. 2, no. 6, pp. 1807–1809, Jun. 1995.

[23] H.-C. Lee and C.-W. Chung, "Comparisons of the electrical characteristics by impedance matching conditions on the E–H and H–E transition and the hysteresis of inductively coupled plasma," *Thin Solid Films*, vol. 521, pp. 185–188, Oct. 2012.

[24] Z. F. Ding, G. Y. Yuan, W. Gao, and J. C. Sun, "Effects of impedance matching network on the discharge mode transitions in a radio-frequency inductively coupled plasma," *Phys. Plasmas*, vol. 15, no. 6, Jun. 2008, Art. no. 063506.

[25] M. A. Razzak, S. Takamura, and Y. Uesugi, "Dynamics of E-H mode transition in high-pressure RF inductively coupled plasmas," *IEEE Trans. Plasma Sci.*, vol. 33, no. 2, pp. 284–285, Apr. 2005.

[26] X. Zhang *et al.*, "The transition mechanisms of the E to H mode and the H to E mode in an inductively coupled argon-mercury mixture discharge," *Phys. Plasmas*, vol. 22, no. 10, Oct. 2015, Art. no. 103509.

[27] F. Anderegg, E. M. Hollmann, and C. F. Driscoll, "Rotating field confinement of pure electron plasmas using Trivelpiece-Gould modes," *Phys. Rev. Lett.*, vol. 81, no. 22, pp. 4875–4878, Nov. 1998.

[28] Y. W. Lee, H. L. Lee, and T. H. Chung, "E-H mode transition in low-pressure inductively coupled nitrogen-argon and oxygen-argon plasmas," *J. Appl. Phys.*, vol. 109, no. 11, Jun. 2011, Art. no. 113302.

[29] H.-C. Lee, J.-K. Lee, and C.-W. Chung, "Evolution of the electron energy distribution and E-H mode transition in inductively coupled nitrogen plasma," *Phys. Plasmas*, vol. 17, no. 3, Mar. 2010, Art. no. 033506.

[30] R. Zaplotnik, A. Vesel, and M. Mozetic, "Transition from E to H mode in inductively coupled oxygen plasma: Hysteresis and the behaviour of oxygen atom density," *Europhys. Lett.*, vol. 95, no. 5, Sep. 2011, Art. no. 55001.

[31] T. Wegner, C. Küllig, and J. Meichsner, "Excitation patterns and heating mechanisms during E-H-mode transition in inductively coupled RF oxygen discharges," *IEEE Trans. Plasma Sci.*, vol. 42, no. 10, pp. 2830–2831, Oct. 2014.

[32] Z. Zhang, X. Zhang, J. Cao, Y. Liu, P. Wang, and P. Yu, "Mode transition in an inductively coupled argon–mercury mixture discharge studied by interferometer and optical emission spectroscopy," *IEEE Trans. Plasma Sci.*, vol. 46, no. 9, pp. 3151–3158, Sep. 2018.

[33] T. Wegner, C. Küllig, and J. Meichsner, "Mode transition and hysteresis in inductively coupled radio frequency argon discharge," *Phys. Plasmas*, vol. 23, no. 2, Feb. 2016, Art. no. 023503.

[34] X. Zhang, Z.-K. Zhang, J.-X. Cao, Y. Liu, and P.-C. Yu, "The influence of gas pressure on E↔H mode transition in argon inductively coupled plasmas," *AIP Adv.*, vol. 8, no. 3, Mar. 2018, Art. no. 035121.

[35] M. M. Turner and M. A. Lieberman, "Hysteresis and the E-to-H transition in radiofrequency inductive discharges," *Plasma Sources Sci. Technol.*, vol. 8, no. 2, pp. 313–324, Jan. 1999.

[36] I. M. El-Fayoumi, I. R. Jones, and M. M. Turner, "Hysteresis in the E- to H-mode transition in a planar coil, inductively coupled RF argon discharge," *J. Phys. D: Appl. Phys.*, vol. 31, no. 21, pp. 3082–3094, Nov. 1998.

[37] M.-H. Lee *et al.*, "On the E to H and H to E transition mechanisms in inductively coupled plasma," *Phys. Plasmas*, vol. 13, no. 6, Jun. 2006, Art. no. 063510

[38] V. I. Kolobov and R. R. Arslanbekov, "Simulation of electron kinetics in gas discharges," *IEEE Trans. Plasma Sci.*, vol. 34, no. 3, pp. 895–909, Jun. 2006.

[39] M.-H. Lee, K. H. Lee, D.-S. Hyun, and C.-W. Chung, "On the hysteresis in E to H and H to E transitions and the multistep ionization in inductively coupled plasma," *Appl. Phys. Lett.*, vol. 90, no. 19, May 2007, Art. no. 191502.

[40] S. V. Singh, P. Kempkes, and H. Soltwisch, "Electron energy distribution function close to the mode transition region in an inductively coupled gaseous electronics conference reference cell," *Appl. Phys. Lett.*, vol. 89, no. 16, Oct. 2006, Art. no. 161501.

[41] I.-S. Park, H.-J. Kang, K.-H. Kim, and C.-W. Chung, "Experimental investigation of edge-to-center density ratio in E-H mode transition of an inductively coupled plasma," *Phys. Plasmas*, vol. 24, no. 12, Dec. 2017, Art. no. 123506.

[42] J. B. Boffard, C. C. Lin, and C. A. DeJoseph, Jr., "Application of excitation cross sections to optical plasma diagnostics," *J. Phys. D: Appl. Phys.*, vol. 37, no. 12, pp. R143–R161, May 2004.

[43] S. V. Singh, "Hysteresis and mode transition in terms of electron energy distribution function for an inductively coupled argon discharge," *J. Appl. Phys.*, vol. 103, no. 8, Apr. 2008, Art. no. 083303.

[44] I. M. El-Fayoumi and I. R. Jones, "Theoretical and experimental investigations of the electromagnetic field within a planar coil, inductively coupled RF plasma source," *Plasma Sources Sci. Technol.*, vol. 7, no. 2, pp. 162–178, May 1998.

[45] A. M. Daltrini, S. A. Moshkalev, T. J. Morgan, R. B. Piejak, and W. G. Graham, "Plasma power measurement and hysteresis in the E–H transition of a RF inductively coupled plasma system," *Appl. Phys. Lett.*, vol. 92, no. 6, Feb. 2008, Art. no. 061504.

[46] F. Gao, S.-X. Zhao, X.-S. Li, and Y.-N. Wang, "Effects of matching network on the hysteresis during E and H mode transitions in argon inductively coupled plasma," *Phys. Plasmas*, vol. 17, no. 10, Oct. 2010, Art. no. 103507.

[47] E. Abdel-Fattah, M. Bazavan, and H. Sugai, "Langmuir probe diagnostics of electron energy distributions with optical emission spectroscopy in capacitively coupled RF discharge in nitrogen," *J. Appl. Phys.*, vol. 110, no. 11, Dec. 2011, Art. no. 113303.

[48] I. D. Sudit and F. F. Chen, "RF compensated probes for high-density discharges," *Plasma Sources Sci. Technol.*, vol. 3, no. 2, pp. 162–168, May 1994.

[49] H. Wang, Z. Zhang, K. Yang, C. Tan, R. Cui, and J. Ouyang, "Axial profiles of argon helicon plasma by optical emission spectroscope and Langmuir probe," *Plasma Sci. Technol.*, vol. 21, no. 7, May 2019, Art. no. 074009.

[50] J. H. Ferziger *et al.*, *Computational Methods for Fluid Dynamics*. Berlin, Germany: Springer, 2012.

[51] T. Czerwiec and D. B. Graves, "Mode transitions in low pressure rare gas cylindrical ICP discharge studied by optical emission spectroscopy," *J. Phys. D: Appl. Phys.*, vol. 37, no. 20, pp. 2827–2840, Oct. 2004.

[52] M. A. Lieberman and A. J. Lichtenberg, *Principles of Plasma Discharges and Materials Processing*. New York, NY, USA: Wiley, 2004.

[53] M.-H. Lee and C.-W. Chung, "Self-consistent global model with multi-step ionizations in inductively coupled plasmas," *Phys. Plasmas*, vol. 12, no. 7, Jul. 2005, Art. no. 073501.

[54] M. V. Malyshev and V. M. Donnelly, "Determination of electron temperatures in plasmas by multiple rare gas optical emission, and implications for advanced actinometry," *J. Vac. Sci. Technol. A: Vac., Surf., Films*, vol. 15, no. 3, pp. 550–558, May 1997.

[55] T. K. Popov, P. Ivanova, M. Dimitrova, J. Kovačič, T. Gyergyek, and M. Čerček, "Langmuir probe measurements of the electron energy distribution function in magnetized gas discharge plasmas," *Plasma Sources Sci. Technol.*, vol. 21, no. 2, Mar. 2012, Art. no. 025004.

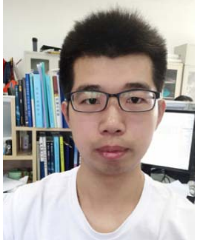

Chuansheng Wang received the B.S. degree in physics from Xiangtan University, Xiangtan, China, in 2017. He is currently pursuing the Ph.D. degree with the State Key Laboratory of High Temperature Gas Dynamics, Institute of Mechanics, Chinese Academy of Sciences (CAS), Beijing, China.

His current research interests include inductively coupled plasma (ICP) discharge, helicon discharge, and diagnostic of plasma.

Xuhui Liu, photograph and biography not available at the time of publication.

Jinyue Geng, photograph and biography not available at the time of publication.

Fei Li was born in Xuzhou, Jiangsu, China, in 1982. He received the B.S. degree from the Department of Modern Mechanics, University of Science and Technology of China, Hefei, China, in 2004, and the Ph.D. degree from the Institute of Mechanics, Chinese Academy of Sciences (CAS), Beijing, China, in 2009.

From 2009 to 2011, he was a Research Assistant with the Institute of Mechanics, CAS. In 2011, he was a Visiting Professor with Virginia Polytechnic Institute and State University, Blacksburg, VA, USA, and Clemson University, Clemson, SC, USA. Since 2012, he has been an Associate Professor with the State Key Laboratory of High-Temperature Gas Dynamics, Institute of Mechanics, CAS. He is the author of more than 60 articles. He holds four patents. His research interests include spectrum measurement technology and its applications, supersonic combustion, new satellite propulsion technology, and radiation characteristics of high enthalpy flow.

Dr. Li has been a member of the Youth Innovation Promotion Association of CAS since 2018.

Xin Lin, photograph and biography not available at the time of publication.

Xilong Yu, photograph and biography not available at the time of publication.